SUPPORTING INFORMATION

Low-Frequency Raman 'Fingerprints' of Two-Dimensional Metal Dichalcogenide Layer Stacking Configurations

Alexander A. Puretzky,*[,†] Liangbo Liang,[‡] Xufan Li,[†] Kai Xiao,[†] Kai Wang,[†] Masoud Mahjouri-Samani,[†] Leonardo Basile[II], Juan Carlos Idrobo,[†] Bobby G. Sumpter,[†,§] Vincent Meunier,[‡] and David B. Geohegan[†]

[†]Center for Nanophase Materials Sciences, Oak Ridge National Laboratory, Oak Ridge, Tennessee 37831, United States

[‡]Department of Physics, Applied Physics, and Astronomy, Rensselaer Polytechnic Institute, Troy, New York 12180, United States

[§]Computer Science and Mathematics Division, Oak Ridge National Laboratory, Oak Ridge, Tennessee 37831, United States

[II]Departamento de Física, Escuela Politécnica Nacional, Quito 170525, Ecuador

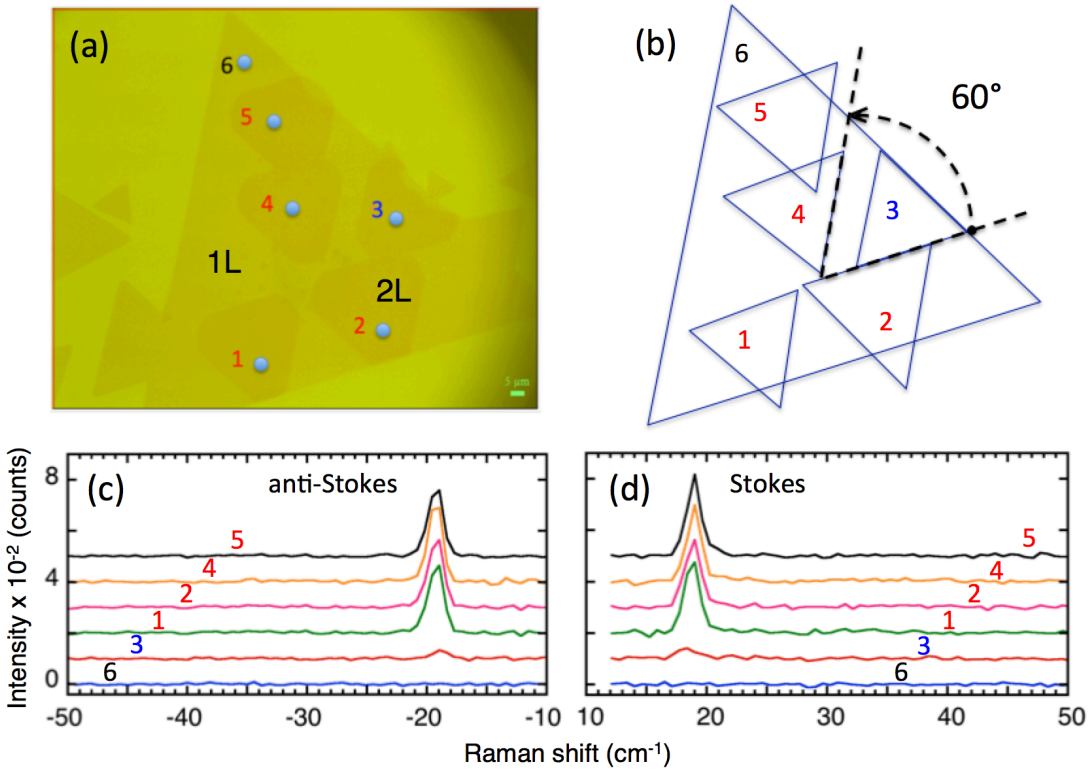

Figure S1. Stokes and anti-Stokes Raman spectra of five 2L $MoSe_2$ crystals measured at points 1-5 and 1L $MoSe_2$ measured at point 6. (**a**) Optical image of a large triangular 1L $MoSe_2$ crystal decorated with 5 small 1L crystals at 60° (points 1, 2, 4, 5) and 0° (point 3) orientations relative to the large one. (**b**) Schematic showing mutual orientation of the triangular $MoSe_2$ crystals. (**c**) Anti-Stokes and (**d**) Stokes Raman spectra measured at the points 1-6 shown in (a).

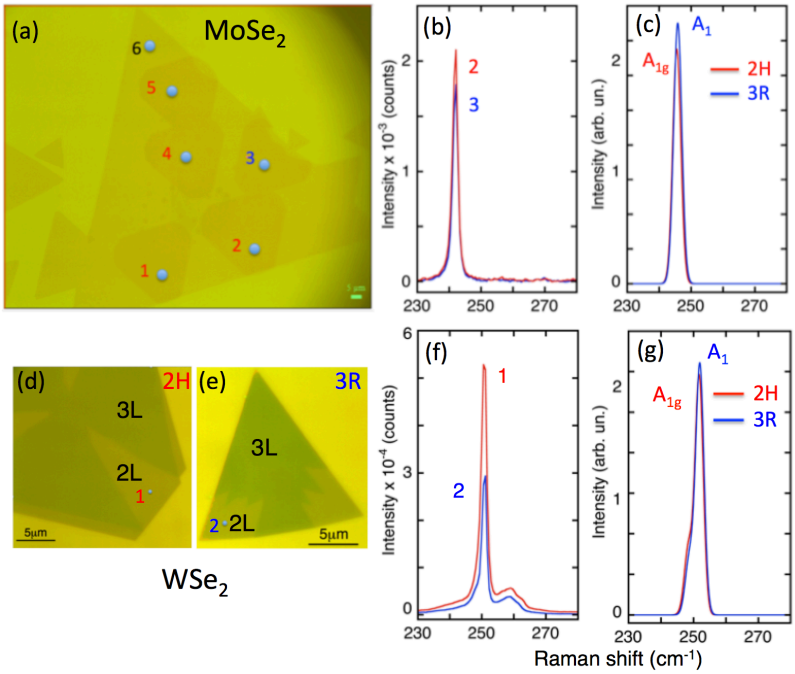

Figure S2. $MoSe_2$ and WSe_2 bilayer Raman spectra for 2H and 3R stacking patterns. All spectra were measured in $\bar{z}(xx)z$ polarization configuration and all samples were synthesized by CVD. (**a**) Optical microscope image of a large 1L $MoSe_2$ crystal decorated with 5 smaller 1L crystals to form 2L $MoSe_2$ with 0° (3R stacking, marked as 3) and 60° (2H stacking, marked as 1, 2, 4, 5) mutual rotations. (**b**) High-frequency (HF) Raman spectra of 2L $MoSe_2$ for 2H (marked as 2) and 3R (marked as 3). (**c**) Calculated HF Raman spectra for 2L $MoSe_2$ for 2H (red) and 3R (blue) stacking configurations. (**d**), (**e**) Optical microscope images of 2-3L WSe_2 crystals in 2H and 3R stacking configurations, respectively for 2L. (**f**) High-frequency Raman spectra of 2L WSe_2 for 2H (marked as 1) and 3R (marked as 2) stacking configurations. (**g**) Calculated HF Raman spectra for 2L WSe_2 for 2H (red) and 3R (blue) stacking configurations.

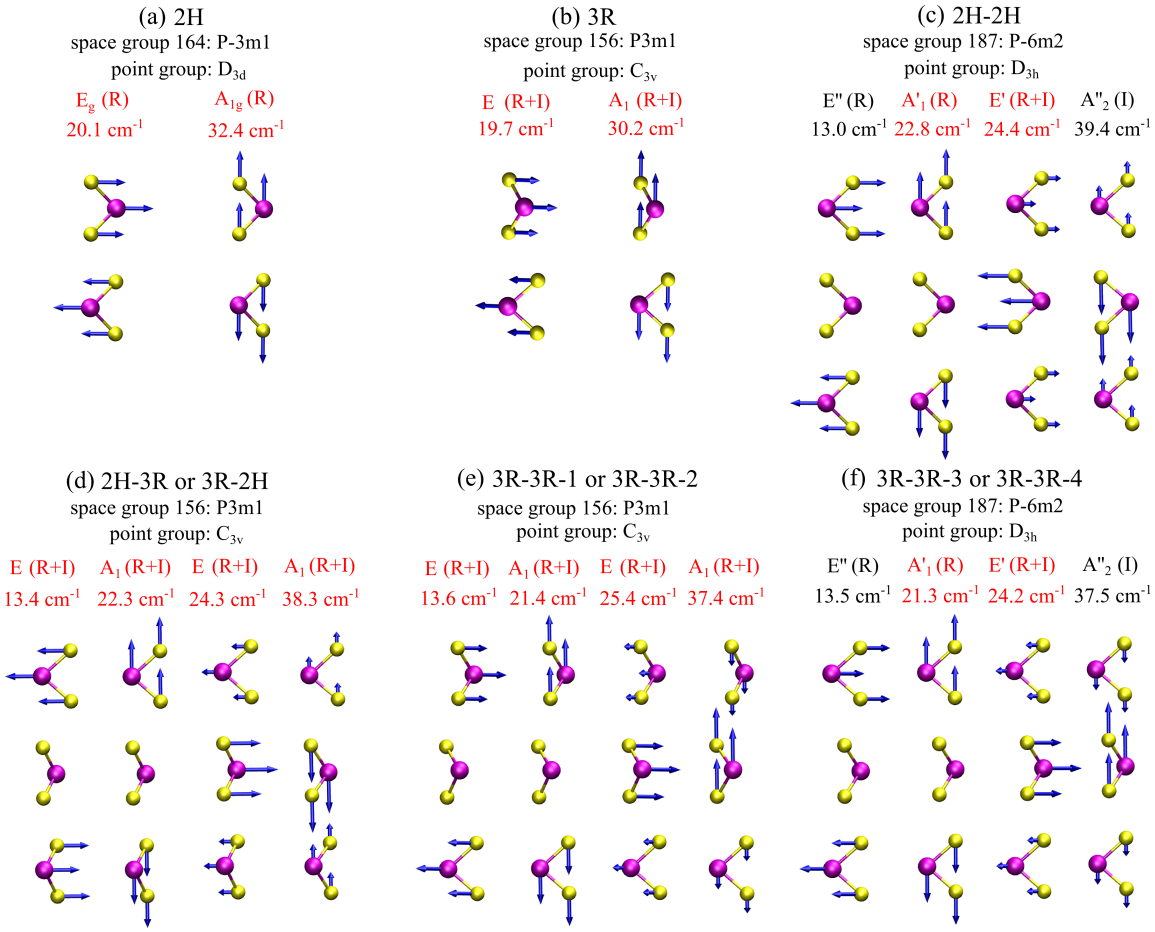

Figure S3. Interlayer in-plane shear and out-of-plane breathing modes in bilayer and trilayer $MoSe_2$ at different stacking patterns. The blue arrows indicate both magnitude and direction of the vibrations. The calculated frequencies are shown as well. A 2L system has 1 double-degenerate interlayer shear mode and 1 interlayer breathing mode, while a 3L system has 2 double-degenerate shear modes and 2 breathing modes. For each stacking, the space group and point group are indicated, which determine the symmetry of each phonon mode and its Raman/infrared activity. The interlayer shear and breathing modes have E and A symmetry, respectively. "R" and "I" indicate the Raman-active and infrared-active, respectively. In the experimental back-scattering geometry, phonon modes that can in principle be observed by our Raman measurements are highlighted in red color. (**a**), (**b**) 2H and 3R stacking configurations for 2L. (**c-f**) 2H and 3R stacking combinations for 3L. In (**d**), 2H-3R is equivalent to 3R-2H. In (**e**) and (**f**), 3R-3R-2 is very similar to 3R-3R-1, and 3R-3R-4 is to 3R-3R-3.

S1. Theory

Group theory analysis and first-principles calculations of Raman scattering of 2L and 3L $MoSe_2$ and 2L WSe_2 at various stacking patterns.

For the interlayer vibrations in 2L TMDs, each tri-layer (e.g., composed of central Mo and two Se sub-layers) moves as a whole unit, while the adjacent tri-layers move in the opposite directions, as illustrated by the blue arrows in Figure S3a. Hence, the frequency of an interlayer phonon mode is determined by the interlayer vdW restoring force and the mass of the layer per unit surface area. The weak nature of vdW interactions renders the frequency typically below 50 cm^{-1} for TMDs[1]. Interlayer phonon modes that correspond to vibrations in the x or y directions are called in-plane shear modes (thus double-degenerate), while those vibrating in the z direction are out-of-plane breathing modes (non-degenerate). In NL TMDs (N is the number of tri-layers), there are $N-1$ double-degenerate interlayer shear modes and $N-1$ interlayer breathing modes[1]. Therefore, a 2L TMD has 1 double-degenerate interlayer shear mode and 1 interlayer breathing mode, while a 3L TMD has 2 double-degenerate shear modes and 2 breathing modes. The symmetries and Raman/infrared activities of these interlayer modes depend on the space and point groups of the stacking configurations, as detailed in Fig. S3. According to the classical Placzek approximation[2,3], the Raman intensity of a phonon mode is proportional to $|e_i \cdot \boldsymbol{\alpha} \cdot e_s|^2$, where e_i and e_s are the electric polarization vectors of the incident and scattered light respectively, and $\boldsymbol{\alpha}$ is the Raman tensor of the phonon mode. Only when $|e_i \cdot \boldsymbol{\alpha} \cdot e_s|^2$ is not zero, can the phonon mode be Raman active. First-principles calculations were performed to obtain Raman tensors, $\boldsymbol{\alpha}$, for interlayer shear and breathing modes at different stacking patterns, as shown below.

For the space group 164, which includes 2L TMDs with 2H stacking (Fig. S3a),

$$\mathrm{E_g}: \begin{pmatrix} a & 0 & 0 \\ 0 & -a & d \\ 0 & d & 0 \end{pmatrix}, \begin{pmatrix} 0 & a & d \\ a & 0 & 0 \\ d & 0 & 0 \end{pmatrix}; \mathrm{A_{1g}}: \begin{pmatrix} b & 0 & 0 \\ 0 & b & 0 \\ 0 & 0 & c \end{pmatrix}. \quad (1)$$

For space group 156, which includes 2L TMDs with 3R stacking and 3L TMDs with 2H-3R and 3R-3R-1 stacking configurations shown in Figs. S3b, d, e,

$$\mathrm{E}: \begin{pmatrix} a & 0 & 0 \\ 0 & -a & d \\ 0 & d & 0 \end{pmatrix}, \begin{pmatrix} 0 & a & d \\ a & 0 & 0 \\ d & 0 & 0 \end{pmatrix}; \mathrm{A_1}: \begin{pmatrix} b & 0 & 0 \\ 0 & b & 0 \\ 0 & 0 & c \end{pmatrix}. \quad (2)$$

For space group 187, which includes 3L TMDs with 2H-2H and 3R-3R-3 stacking configurations presented in Figs. S3c, f,

$$\mathrm{E'}: \begin{pmatrix} a & 0 & 0 \\ 0 & -a & 0 \\ 0 & 0 & 0 \end{pmatrix}, \begin{pmatrix} 0 & a & 0 \\ a & 0 & 0 \\ 0 & 0 & 0 \end{pmatrix}; \mathrm{A'_1}: \begin{pmatrix} b & 0 & 0 \\ 0 & b & 0 \\ 0 & 0 & c \end{pmatrix};$$

$$\mathrm{E''}: \begin{pmatrix} 0 & 0 & 0 \\ 0 & 0 & d \\ 0 & d & 0 \end{pmatrix}, \begin{pmatrix} 0 & 0 & d \\ 0 & 0 & 0 \\ d & 0 & 0 \end{pmatrix}; \mathrm{A''_2}: \begin{pmatrix} 0 & 0 & 0 \\ 0 & 0 & 0 \\ 0 & 0 & 0 \end{pmatrix}. \quad (3)$$

The calculated Raman tensors shown above can also be qualitatively predicted by group theory analysis based on the symmetry (see "Bilbao Crystallographic Server")[4,5]. However, obtaining the numerical values for the Raman tensor elements by *ab initio* calculations are crucial to the understanding of stacking-induced intensity changes in experimental LF Raman spectra of 2D TMDs.

For 2L $MoSe_2$, from 2H to 3R stacking, the measured frequency of the interlayer shear mode slightly decreases while its intensity drops significantly, as discussed previously in Fig. 2b of the main text. The frequency decrease is probably due to the slight weakening of the interlayer coupling. However, the reason for the intensity drop is not immediately clear. According to Eqs. 1, 2, although the symmetry of the shear mode changes from E_g to E, the form of its Raman tensor remains unchanged from 2H to 3R. But the magnitude of matrix element a in the Raman tensor is decreased from 0.234 to 0.141 (in the unit of $Å^2/\sqrt{a.m.u}$) due to the stacking change. In the parallel $\bar{z}(xx)z$ laser polarization configuration, the intensity, I, of the shear mode is proportional to a^2. Therefore, the calculated intensity is decreased by a factor of 2.7, accounting for the measured intensity drop of the shear mode. Similarly for 2L WSe_2, from 2H to 3R, the matrix element, a, is decreased from 0.156 to 0.077, confirming the measured intensity drop of the shear mode in Fig. 2f. However, the symmetry of the breathing mode changed from A_{1g} to A_1 and the matrix element b is increased from 0.146 to 0.255 (Eqs. 1, 2) leading to a large increase of the intensity by a factor of 3.1 since $I \propto b^2$ for $\bar{z}(xx)z$ polarization configuration. This is consistent with the measured increase of the breathing mode intensity in 2L WSe_2 (Fig. 2f). It is also interesting to note that the forms of the Raman tensors of LF breathing modes and HF out-of-plane Raman modes (A_{1g}, A_1 or A'_1) dictate that they can only be observed under the $\bar{z}(xx)z$ polarization configuration and will be completely disappeared under the perpendicular $\bar{z}(xy)z$ configuration[1].

According to the Raman tensor analysis above, a remarkable stacking-induced change in 3L $MoSe_2$ is due to the change of the symmetries that can be described by the corresponding Raman tensors of two shear modes at ~ 13 and ~ 24 cm^{-1} (Eq. 2 and Eq. 3). For 2H-2H (Fig. S3c) or 3R-3R-3 (Fig. S3f) stacking configurations the shear mode near 13 cm^{-1} has symmetry E″ and its Raman tensor determines that it has zero Raman intensities under the experimental back-scattering geometry (Eq. 3); for 2H-3R stacking configurations (Fig. S3d) and 3R-3R-1 (Fig. S3e), the shear mode near 13 cm^{-1} switches symmetry to E and its intensity becomes non-zero (Eq. 2). Thus, the shear mode around 13 cm^{-1} is an obvious fingerprint to differentiate the stacking patterns of 3L $MoSe_2$, as shown in Fig. 4 and Fig. S9. In addition, although 2H-3R (Fig. S3d) and 3R-3R-1 (Fig. S3e) stacking configurations share the same symmetry group and same form of Raman tensors (Eq. 2), the magnitudes of matrix elements in Raman tensors are different. For the shear mode E near 13 cm^{-1}, the matrix element a is 0.195 for 2H-3R while it is 0.139 for 3R-3R-1; for the shear mode E near 24 cm^{-1}, the matrix element a is 0.077 for 2H-3R while it is only 0.002 for 3R-3R-1. Since $I \propto a^2$, the shear mode near 24 cm^{-1} of 3R-3R-1 has very small intensity and thus practically cannot be observed. Consequently, the higher-frequency shear mode around 24 cm^{-1} can also be used to further differentiate the stacking patterns 2H-3R and 3R-3R-1, as discussed in the main text (Figs. 4b and 4c; Figs. S9b and S9c).

Table S1. Frequencies and relative intensities of LF Raman shear and breathing modes and HF in-plane and out-of-plane modes for 2L WSe_2 with 2H and 3R stacking patterns. The frequencies and intensities in the parentheses (*italic*) correspond to theoretical values. All intensities are normalized to the intensity of 521cm^{-1} Si peak. The laser excitation power at the sample location was 65 μW. Note that for 2L TMDs, at 2H stacking, HF in-plane and out-of-plane modes have symmetries E_g and A_{1g}; at 3R stacking, they have symmetries E and A_1.

2L WSe_2 stacking patterns		LF modes		HF modes	
		Shear *ω(cm^{-1})/I*	Breathing *ω(cm^{-1})/I*	In-plane *ω(cm^{-1})/I*	Out-of-plane *ω(cm^{-1})/I*
2H	Experiment	16.9/0.093	28.8/0.093	249.1/2.6	250.7/9.2
	Theory	(*17.7*)/(*12.2*)	(*27.2*)/(*4.7*)	(*248.4*)/(*16.2*)	(*251.8*)/(*58.7*)
3R	Experiment	15.8/0.029	27.3/0.19	249.0/1.4	250.8/4.5
	Theory	(*16.4*)/(*3.45*)	(*25.1*)/(*14.6*)	(*248.7*)/(*13.5*)	(*252.0*)/(*61.0*)

Table S2. Summary of the frequencies for shear, breathing LF, and out-of-plane and in-plane HF modes measured for 2L $MoSe_2$ crystals synthesized in different experiments described in Methods section in the main text. The frequencies in italic in the parentheses correspond to theoretical values. Note that for 2L TMDs, at 2H stacking, HF in-plane and out-of-plane modes have symmetries E_g and A_{1g}; at 3R stacking, they have symmetries E and A_1.

2L $MoSe_2$ stacking patterns, experiments, and (number of analyzed crystals)		LF modes (cm^{-1})		HF modes (cm^{-1})	
		Shear	Breathing	Out-of-plane	In-plane
2H	Exp.1 (4)	19.0±0.1		241.9±0.1	~285
	Exp.2 (7)	19.1±0.1		241.9±0.2	
	Exp.3WG** (3)	19.1±0.1		242.4±0.2	
	Exp.4 (4)	19.2±0.1		242.0±0.1	
	Exp.5 (3)	19.2±0.1			
	Exp.6W* (5)	19.3±0.1		242.9±0.1	
	Exp.7(12)	19.5±0.1	34.2±0.2	241.8±0.1	
	Exp.8 Exf.***(2)	19.4±0.1		242.3±0.1	286.7
	Theory	*20.1*	*32.4*	*245.6*	*289.2*
3R	Exp.1 (7)	18.5±0.2		242.2±0.1	~285
	Exp.2 (2)	18.5±0.1		242.2±0.1	
	Exp.3WG** (4)	18.7±0.1		242.4±0.2	
	Exp.4 (1)	18.6		242.0	
	Exp.5 (3)	18.7±0.2			
	Exp.6W* (7)	19.0±0.1		242.9±0.3	
	Exp.7(8)	19.1±0.1		242.0±0.2	
	Theory	*19.7*	*30.2*	*245.9*	*289.6*

* W doped $MoSe_2$
** W doped $MoSe_2$ suspended on a TEM grid
***Exfoliated $MoSe_2$

S2. Excitation laser power dependence of the LF Raman spectra of 2L $MoSe_2$ on a SiO_2/Si substrate and suspended on a SiN TEM grid: damage thresholds.

To understand how incident laser power effects the positions and linewidths of the low frequency modes in 2L $MoSe_2$ we measured LF Raman spectra in the wide range of the excitation laser powers from 8μW to 2mW for the sample on a SiO_2/Si substrate (Exp. 2, Table S2). We found that the intensity of the shear mode increased linearly with the laser power and its peak position and the linewidth did not change in the range of laser powers from 8 μW to 1 mW (Figure S4). This indicates that no substantial heating of the sample occurred at these laser powers. At laser power higher than 1 mW a sharp deviation from the linearity together with degradation of the sample at the irradiated point was observed.

However, in the case of 2L $MoSe_2$ crystals suspended on a TEM grid (Figure S5) the damage threshold decreased ~ 3 times to 0.3 mW compared to the same 2D crystals on SiO_2/Si substrates. Therefore, in this case the excitation laser power, used to acquire the LF Raman spectra, was reduced to 55 μW. The STEM images of the 2L $MoSe_2$ area damaged during spectra acquisition at 0.3 mW excitation laser power show interesting triangular shaped laser thinning from 2L to 1L patterns and also formation of triangular holes (Figures. S6a, b). The spectra measured at 0.3 mW show broadening and red shifts (~ 0.6 cm^{-1} for LF- and ~ 0.9 cm^{-1} for HF-modes, respectively), probably due to anharmonic shift and broadening upon laser heating (Figs. S6c, d).

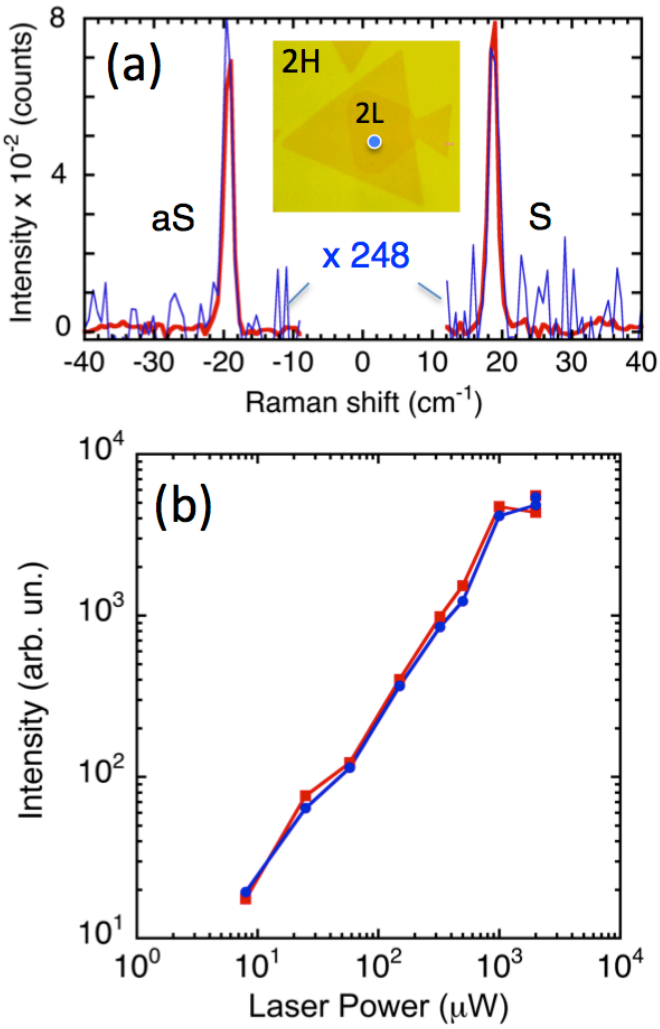

Figure S4. Excitation laser power dependence of the LF Raman spectrum of 2L $MoSe_2$ showing no difference in the positions and linewidths of the shear LF-mode at 19.1 cm^{-1}. (**a**) Stokes and anti-Stokes Raman spectra of 2L $MoSe_2$ crystals (2H stacking) synthesized in Experiment 2 and measured at 8 μW (blue curve) and 1mW (red curve) excitation laser powers. The intensity of the 8μW-spectrum is multiplied by a factor of 248 to normalize the spectra. Insert shows an optical microscope image with the position of the excitation laser beam marked by a circle. (**b**) Peak intensity of the 19.1cm^{-1} Raman line versus excitation laser power.

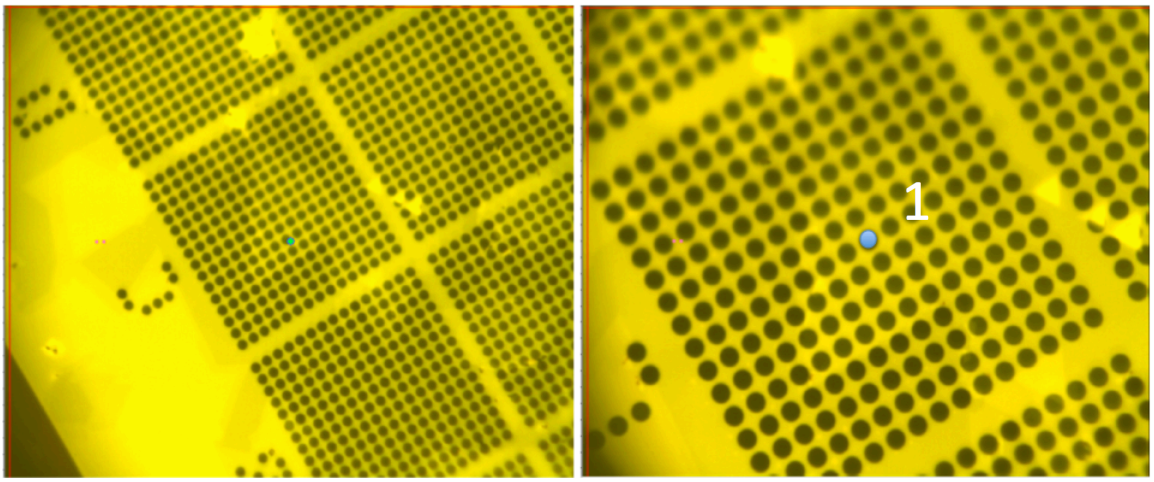

Figure S5. Optical microscope images of the TEM grid used for combined Raman and atomic resolution STEM measurements. (right) An example of magnified image of square C1 (left) with the location of the 2μm hole 1 (marked with a circle) used for both measurements.

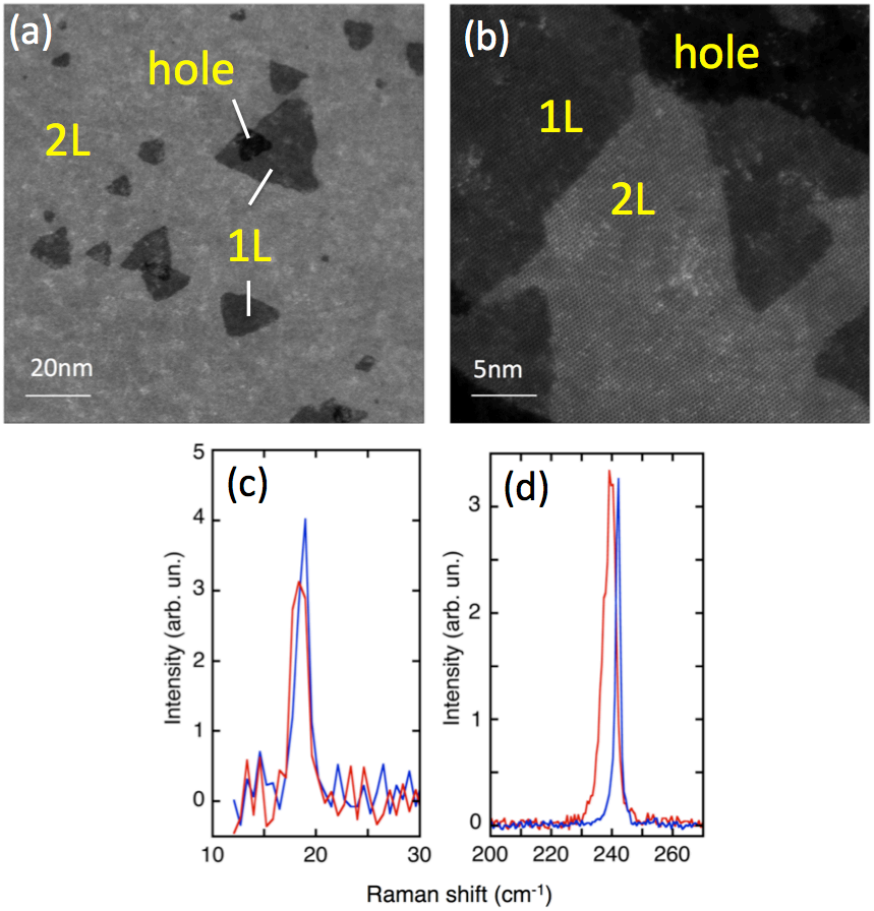

Figure S6. Evidence of induced damage for the 2L $MoSe_2$ crystals at 0.3 mW excitation laser power. (**a**), (**b**) STEM images of the 2L $MoSe_2$ area damaged during spectra acquisition showing triangular shaped laser thinning pattern from 2L to 1L and formation of triangular holes. (**c**), (**d**) Raman spectra for LF shear and HF modes, respectively acquired using 0.3 mW excitation laser power (red curves). The corresponding spectra measured at 55 μW where no damage occurred are shown for comparison (blue curves). The spectra measured at 0.3 mW show broadening and red shifts (~ 0.6 cm^{-1} for LF- and ~ 0.9 cm^{-1} for HF-modes, respectively), probably due to anharmonic shift and broadening upon laser heating.

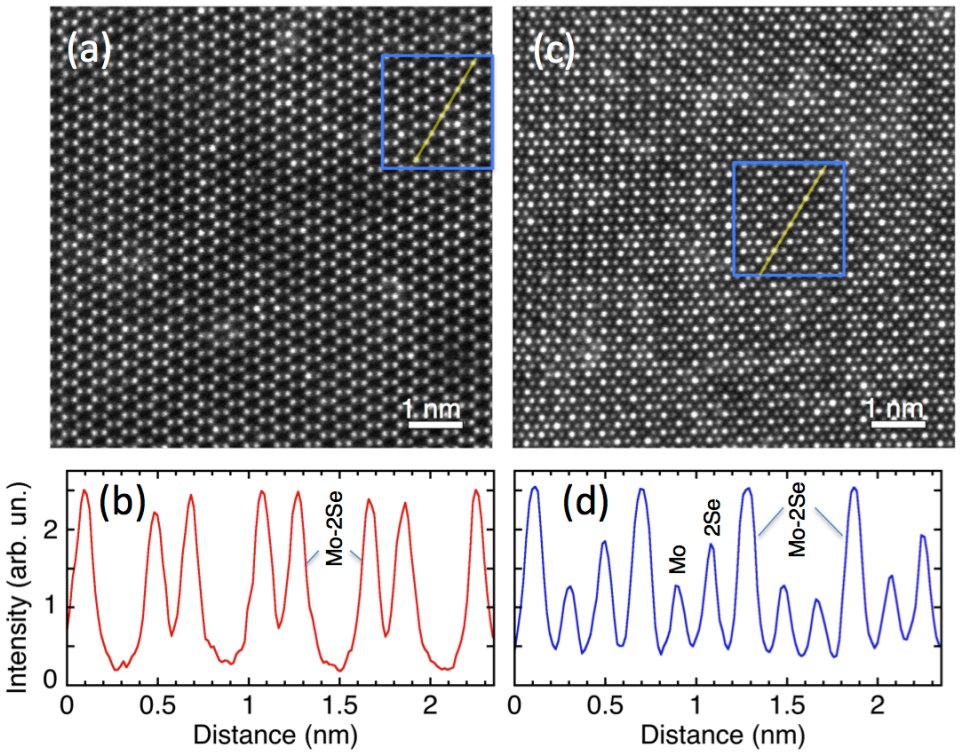

Figure S7. Atomic resolution STEM images of 2L $MoSe_2$ showing 2H and 3R stacking patterns. (**a**) (**c**) ADF-STEM images of 2L $MoSe_2$ in the 2H and 3R stacking configurations, respectively with the corresponding intensity line profiles (**b**), (**d**) measured along the lines shown in the inserts to (a) and (c).

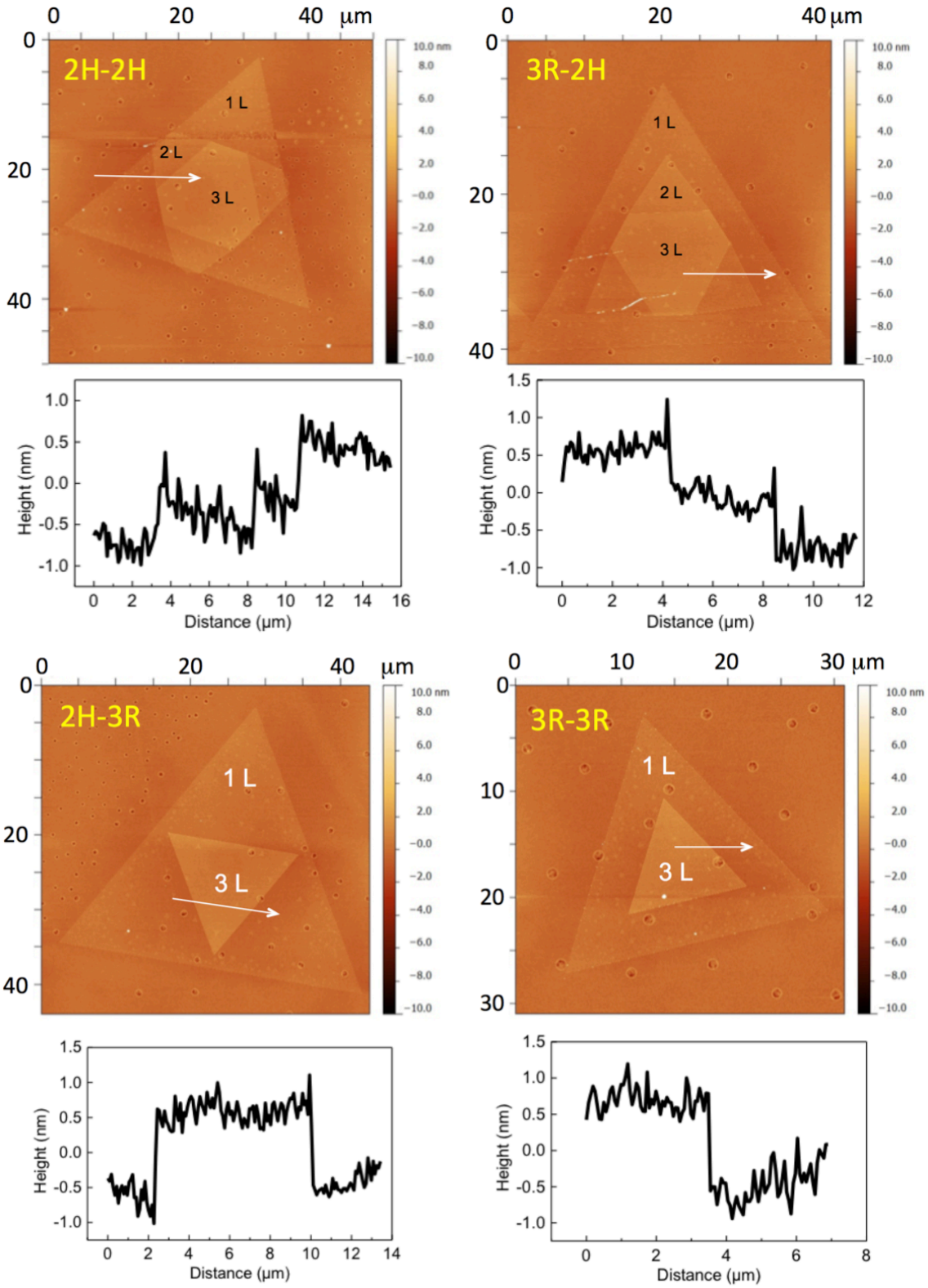

Figure S8. AFM images of 3L MoSe2 crystals with 2H-2H, 3R-2H, 2H-3R, and 3R-3R stacking configurations and the corresponding height profiles used to determine the number of layers.

Table S3. Summary of Raman frequencies of low-frequency (LF) shear modes and high-frequency (HF) out-of-plane modes for 3L $MoSe_2$ with different stacking patterns. The frequencies in italic in the parentheses are the corresponding theoretical values. Note that starting from 3 layers, Davydov splitting of the HF Raman line leads to two components, as widely reported in the literature. For 3L $MoSe_2$ samples, the LF breathing modes are very weak and are not observed in our experiments. The frequency of the HF in-plane mode was ~ 286 cm^{-1} and its intensity is also very low. Note that for 3L TMDs, depending on the stacking patterns, HF out-of-plane mode can have symmetry either A'_1 or A_1, and HF in-plane mode can have symmetry either E′ or E (see Fig. S3 for more details).

3L $MoSe_2$ stacking patterns		LF shear modes (cm^{-1})		HF out-of-plane modes (cm^{-1})	
2H-2H	Exp.1 (5)		24.0±0.1 (*24.4*)	239.3±0.2 (*243.5*)	242.5±0.2 (*245.8*)
2H-3R	Exp.1 (7)	14.0±0.1 (*13.4*)	23.4±0.1 (*24.3*)	239.6±0.2 (*243.7*)	242.8±0.2 (*246.0*)
3R-2H	Exp.1 (6)	14.0±0.1 (*13.4*)	23.4±0.1 (*24.3*)	239.7±0.2 (*243.7*)	242.6±0.2 (*246.0*)
3R-3R	Exp.1 (3) Exp.2 (5)	13.8±0.1 13.7±0.1 (*13.6*)		239.4±0.2 239.6±0.2 (*243.8*)	242.9±0.2 243.0±0.2 (*246.2*)
3R-3R	Exp.2 (3)		23.1±0.2 (*24.2*)	239.6±0.2 (*243.8*)	243.0±0.2 (*246.3*)

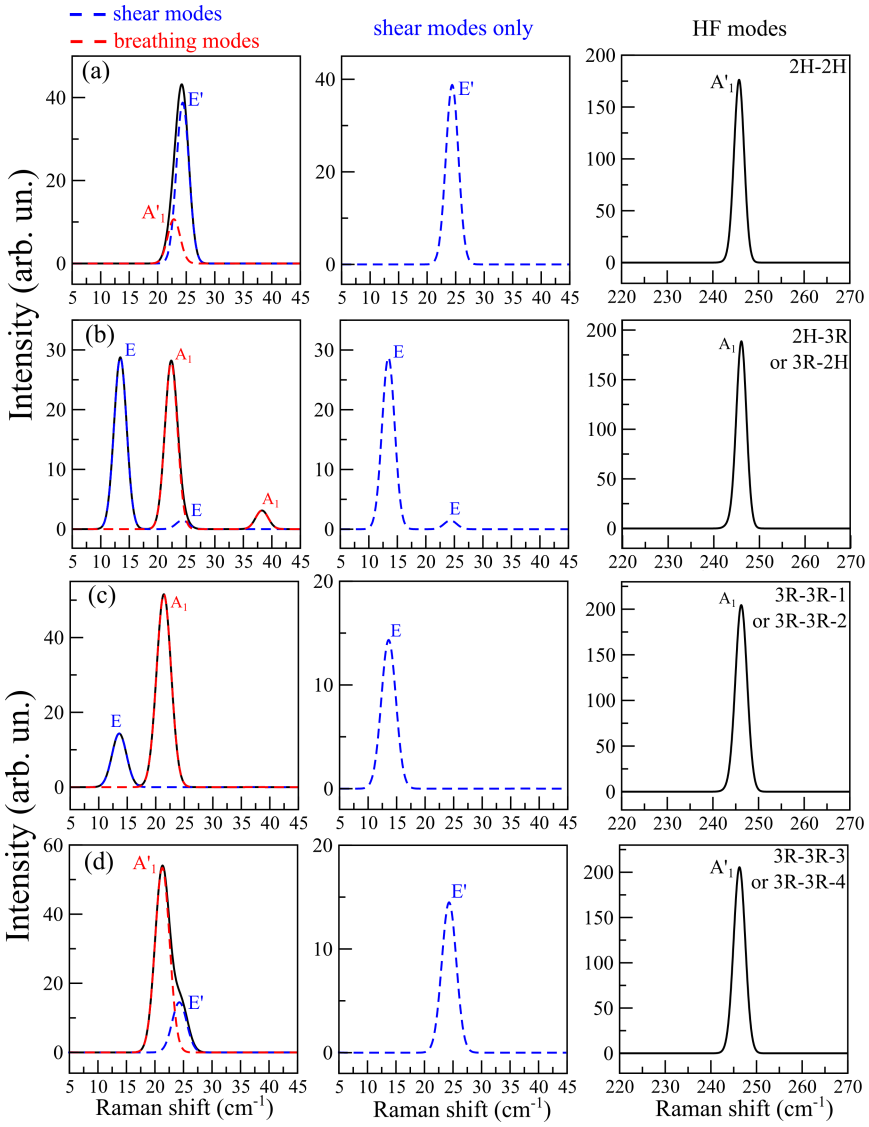

Figure S9. Calculated Raman spectra of 3L $MoSe_2$ at different stacking configurations. (**a**) 2H-2H, (**b**) 2H-3R or 3R-2H, (**c**) 3R-3R-1 or 3R-3R-2, (**d**) 3R-3R-3 or 3R-3R-4 stacking configurations. For each stacking pattern, the low-frequency Raman spectrum is shown in the left panel (black solid line), where the contribution from interlayer shear (breathing) modes is also plotted separately with a blue (red) dashed line. The middle panel only shows Raman signals of the interlayer shear modes since the breathing modes are too weak to be observable experimentally. The high-frequency Raman spectrum of each stacking is presented in the right panel in black solid line. The symmetry of each Raman peak is assigned according to the group theory detailed in Fig. S3.

S3. Polarized Raman measurements of 3L $MoSe_2$ with different stacking patterns.

The possibility of varying light polarization in Raman spectroscopy provides additional valuable information to assign the LF modes for 3L $MoSe_2$. Figures S10a-c show an example of Raman spectra of LF and HF modes for 3L $MoSe_2$ in the case of 2H-2H, 3R-2H, and 3R-3R stacking patterns measured in $\bar{z}(xx)z$ and $\bar{z}(xy)z$ polarization configurations. As expected, the HF A'_1 or A_1 modes disappear under the $\bar{z}(xy)z$ configuration.[1,6] The intensities of the LF modes increased significantly for the 2H-2H and 3R-3R stacking patterns under the $\bar{z}(xy)z$ polarization configuration (Figs. S10a, S10c) and they remained essentially unchanged for the 3R-2H stacking (Fig. S10b) under both polarization configurations. The observed polarization changes in the LF and HF modes can be related either to their symmetries, as in the case of the HF modes, or to 2D crystal orientation relative to the polarization of the incident laser. To determine which of these two possibilities account for the LF mode measurements, we rotated the 3L 2D crystals relative to the fixed polarization of the incident light and measured Raman spectra in the $\bar{z}(xy)z$ and $\bar{z}(xx)z$ polarization configurations. Figures S10d, e show the angular dependence of the absolute intensities and their ratio, respectively for the 24.0 cm^{-1} LF mode for $\bar{z}(xx)z$ and $\bar{z}(xy)z$ polarization configurations in the case of the 2H-2H stacking. Strong dependence of the 24.0 cm^{-1} peak intensity on the rotation angle was observed in the $\bar{z}(xx)z$ polarization configuration, but in the $\bar{z}(xy)z$ configuration its intensity varied only slightly. For example, for the angle close to 60°, the measured intensity of this LF mode remains the same for both polarization configurations, however, for the $\bar{z}(xx)z$ configuration and 30° the intensity drops by a factor of 2 and even more (~18 times) for the 10° rotation. This allows us to attribute the observed difference in the intensities of the LF modes to different crystal orientations, which were selected randomly for the Raman measurements shown in Figs. S10a-c. From this we can conclude that the observed LF modes are interlayer shear modes, since the interlayer breathing modes have zero intensities and cannot be observed under the perpendicular $\bar{z}(xy)z$ polarization configuration like the HF A'_1 or A_1 modes[1]. In addition, the observation of the strong dependence of the Raman intensities on the rotation angle for the $\bar{z}(xx)z$ polarization configuration may provide a simple way to measure crystal orientation of 2D sheets using micro-Raman spectroscopy. As discussed before for 2L $MoSe_2$, its interlayer breathing modes are too weak and cannot be observed. Clearly for 3L $MoSe_2$, the breathing modes are non-detectable as well, even under the parallel $\bar{z}(xx)z$ configuration.

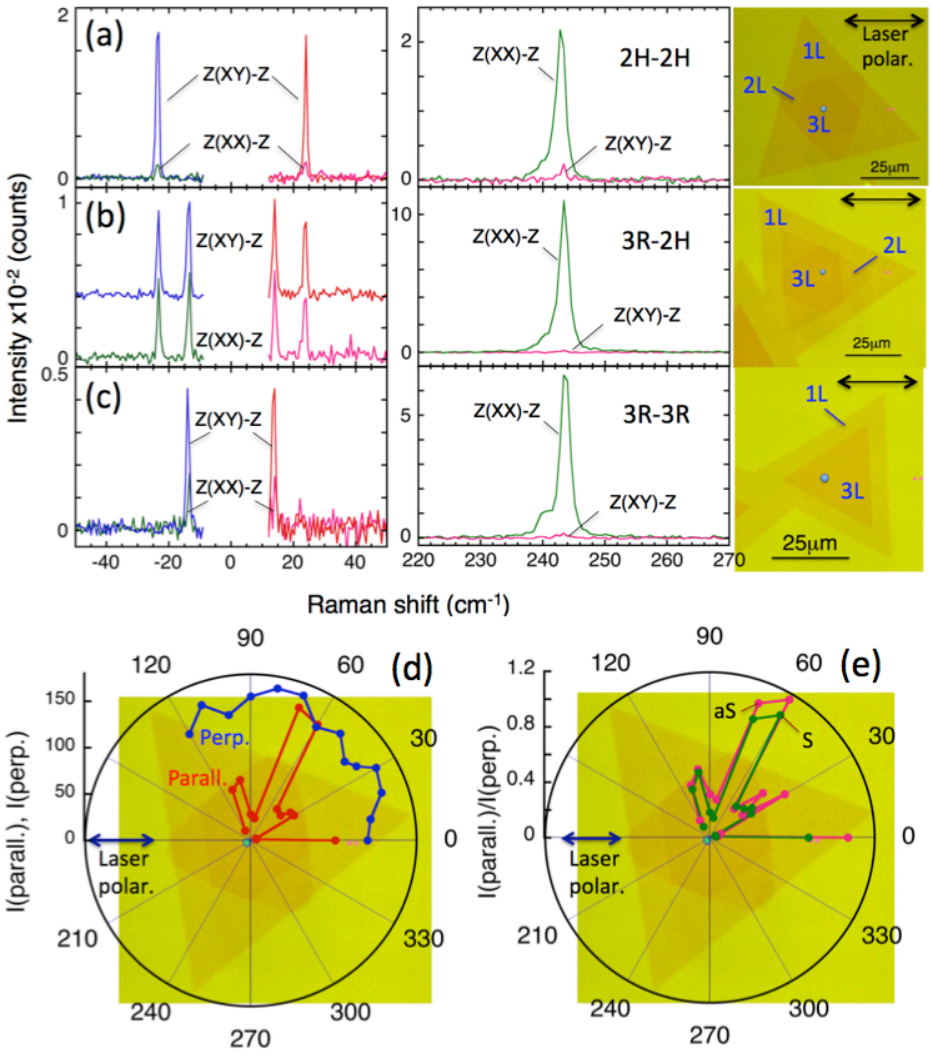

Figure S10. Polarized Raman measurements for different stacking configurations in 3L $MoSe_2$. A set of Raman spectra for LF and HF modes of 3L $MoSe_2$ measured using $\bar{z}(xx)z$ and $\bar{z}(xy)z$ polarization configurations. Images at the right show the corresponding optical images of these 3L structures and the direction of the incident light polarization, which was fixed. (**a**) 2H-2H, (**b**) 2H-3R, (**c**) 3R-3R stacking configurations. (**d**) Polar plot of the peak intensities of the 24 cm^{-1} Raman line [shown in (**a**)] for parallel, $[\bar{z}(xx)z]$, and perpendicular, $[\bar{z}(xy)z]$, polarization configurations versus the sample rotation angle. (**e**) The ratio of the peak intensities, I(parall.)/I(perp.), versus the rotation angle.

Table S4. Summary of the peak intensity ratios of the LF shear mode to the out-of-plane HF mode, I_{LF}(shear)/I_{HF}(out-of-plane), measured for 2L $MoSe_2$ crystals synthesized in different experiments described in Methods section in the main text. The corresponding frequencies of these modes are listed in Table S2. Raman measurements were conducted using parallel, $[\bar{z}(xx)z]$ polarization configuration.

2L $MoSe_2$ stacking patterns, experiments, and (number of analyzed crystals)		I_{LF}(shear)/ I_{HF}(out-of-plane)
2H	Exp.1 (4)	0.11±0.03
	Exp.2 (7)	0.13±0.01
	Exp.3WG** (3)	0.10±0.01
	Exp.4 (4)	0.11±0.03
	Exp.5 (3)	0.10±0.03
	Exp.6W* (5)	0.18±0.02
	Exp.7(12)	0.12±0.01
3R	Exp.1 (7)	0.019±0.004
	Exp.2 (2)	0.021±0.004
	Exp.3WG** (4)	0.021±0.004
	Exp.4 (1)	0.019±0.004
	Exp.5 (5)	0.015±0.006
	Exp.6W* (7)	0.026±0.006
	Exp.7(8)	0.021±0.002

* W doped $MoSe_2$
** W doped $MoSe_2$ suspended on a TEM grid

Table S5. Summary of peak intensity ratios of low-frequency (LF) shear modes and high-frequency (HF) out-of-plane modes, I_{LF} /I_{HF} (242 cm^{-1}), for 3L $MoSe_2$ with different stacking patterns. The corresponding frequencies for all modes are listed in Table S3. Raman measurements were conducted using parallel, [$\bar{z}(xx)z$] polarization configuration.

3L $MoSe_2$ stacking patterns (number of crystals)		LF shear modes (cm^{-1}) (I_{LF} /$I_{HF,\ 242cm^{-1}}$)	
2H-2H	Exp.1 (5)		24.0±0.1 (0.094±0.002)
2H-3R	Exp.1 (7)	14.0±0.1 (0.046±0.006)	23.4±0.1 (0.044±0.004)
3R-2H	Exp.1 (6)	14.0±0.1 (0.049±0.008)	23.4±0.1 (0.046±0.006)
3R-3R	Exp.1 (3) Exp.2 (5)	13.8±0.1 13.7±0.1 (0.027±0.002)	
3R-3R	Exp.2 (3)		23.1±0.2 (0.027±0.004)

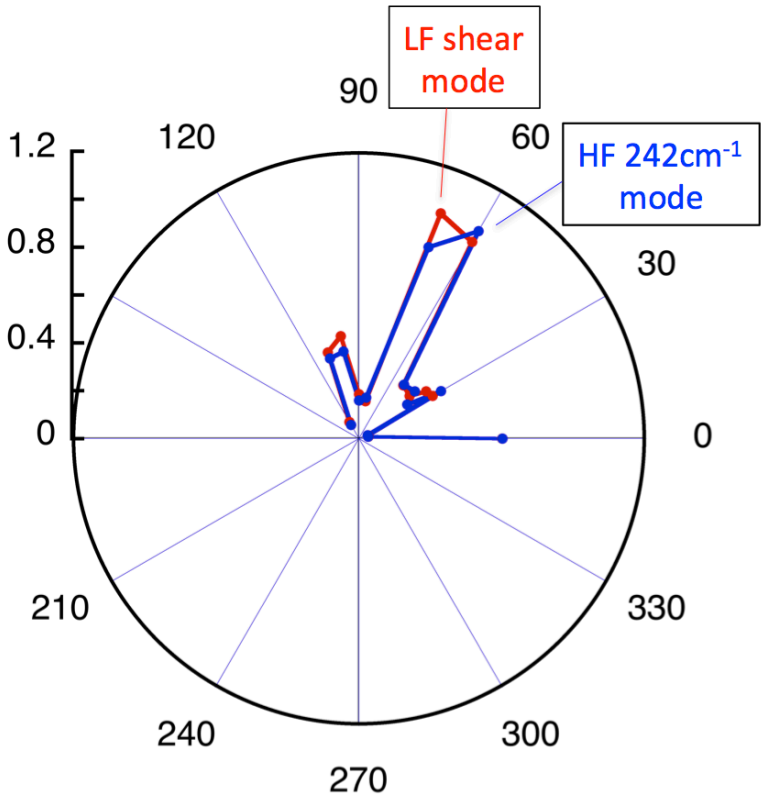

Figure S11. Comparison of the normalized peak intensities of the LF shear and the HF (242 cm^{-1}) Raman modes for 3L $MoSe_2$ in the case of 2H-2H stacking configuration at different sample rotation angles. Polar plot of the normalized peak intensities of the 24 cm^{-1} Raman line (red) and 242 cm^{-1} HF line (blue) [shown in Fig. S10a] for parallel, $[\bar{z}(xx)z]$ polarization configuration versus the sample rotation angle. Clearly, I_{LF} and I_{HF} show the identical behavior *versus* the sample rotation angle, and hence their ratio is independent on the crystal orientation.

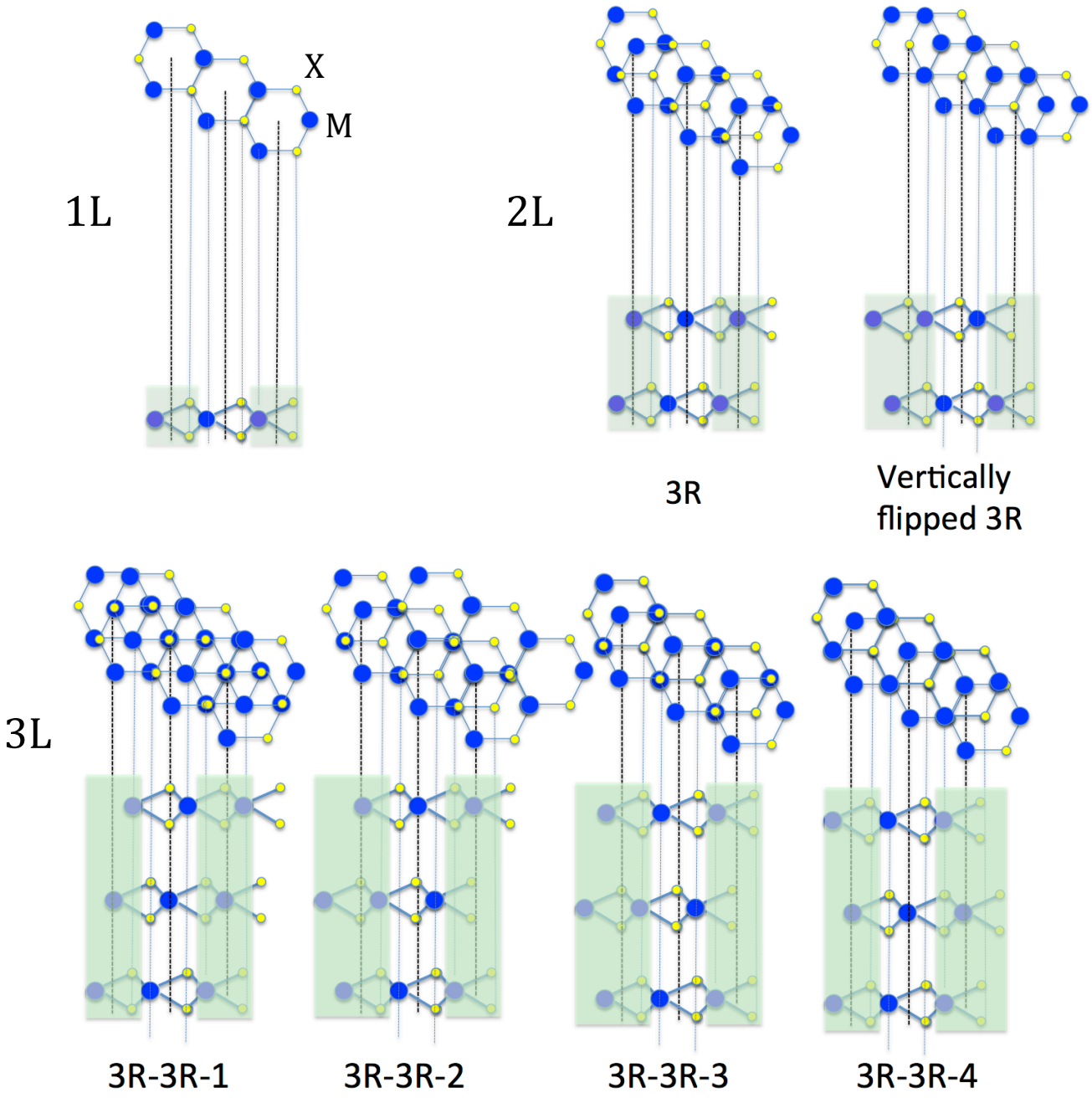

Figure S12. Top and side views of 1L, 2L (3R stacking), and 3L (3R-3R stackings) TMDs. M stands for Mo or W, and X for S or Se. Two possible 3R stackings between the bottom and middle layers, and two possible 3R stackings between the middle and top layers yield the four sub-patterns of 3R-3R. When the 3R stacking between the bottom and middle layers corresponds to bottom M over middle X, and bottom X and middle M aligned with the respective hexagon centers (marked by black dotted lines) of the adjacent layers, the two 3R stackings between the middle and top layers are: middle M over top X, and middle X and top M aligned with the adjacent layers' hexagon centers (3R-3R-1); middle X over top M, and middle M and top X aligned with the adjacent layer hexagon centers (3R-3R-4). Similarly, when the 3R stacking between the bottom and middle layers corresponds to bottom X over middle M, and bottom M and middle X aligned with the adjacent layer hexagon centers, the two 3R stackings between the middle and top layers are: middle X over top M, and middle M and top X aligned with the adjacent layer hexagon centers (3R-3R-2); middle M over top X, and middle X and top M aligned with the adjacent layer hexagon centers (3R-3R-3).

S4. Theoretical lattice constants and atomic coordinates of studied stacking patterns of $MoSe_2$.

Here we provide the theoretical lattice constants and atomic coordinates of studied stacking patterns of $MoSe_2$ in the format of VASP CONTCAR. MoS_2, WS_2 and WSe_2 have similar stacking patterns and structural parameters. Note that atomic coordinates are fractional (or direct) coordinates with respect to the lattice constants.

2L: 2H

```
  1.00000000000000
    3.2538758749999999    0.0000000000000000    0.0000000000000000
   -1.6269379369999999    2.8179391680000001    0.0000000000000000
    0.0000000000000000    0.0000000000000000   28.0000000000000000
  Mo   Se
    2    4
Direct
 0.3333333332308897  0.6666666666666643  0.3863204248589072
 0.6666666664617793  0.3333333333333357  0.6136795751053736
 0.6666666664617793  0.3333333333333357  0.3270370000268352
 0.6666666664617793  0.3333333333333357  0.4457563286846612
 0.3333333332308897  0.6666666666666643  0.5542436712796270
 0.3333333332308897  0.6666666666666643  0.6729629999374529
```

2L: 3R

```
  1.00000000000000
    3.2538758749999999    0.0000000000000000    0.0000000000000000
   -1.6269379369999999    2.8179391680000001    0.0000000000000000
    0.0000000000000000    0.0000000000000000   28.0000000000000000
  Mo   Se
    2    4
Direct
 0.3333333333333357  0.6666666666666643  0.6132659807349653
 0.6666666666666643  0.3333333333333357  0.3866973187936518
 0.6666666666666643  0.3333333333333357  0.6725118216437175
 0.6666666666666643  0.3333333333333357  0.5539796514406216
 0.0000000000000000  0.0000000000000000  0.4460480177115737
 0.0000000000000000  0.0000000000000000  0.3274972097469008
```

3L: 2H-2H

```
  1.00000000000000
    3.2538758745571852    0.0000000000000000    0.0000000000000000
   -1.6269379372785926    2.8179391681278294    0.0000000000000000
    0.0000000000000000    0.0000000000000000   34.0000000000000000
  Mo   Se
    3    6
Direct
 0.3333333333333357  0.6666666666666643  0.6873251356490256
 0.6666666666666643  0.3333333333333357  0.5000000000000000
 0.3333333333333357  0.6666666666666643  0.3126748643509745
 0.6666666666666643  0.3333333333333357  0.7361467328558755
 0.6666666666666643  0.3333333333333357  0.6383773082787638
 0.3333333333333357  0.6666666666666643  0.5489283190549791
```

0.3333333333333357 0.6666666666666643 0.4510716809450209
0.6666666666666643 0.3333333333333357 0.3616226917212362
0.6666666666666643 0.3333333333333357 0.2638532671441245

3L: 2H-3R

1.00000000000000
3.2538758745571852 0.0000000000000000 0.0000000000000000
-1.6269379372785926 2.8179391681278294 0.0000000000000000
0.0000000000000000 0.0000000000000000 34.0000000000000000
Mo Se
3 6
Direct
0.3333333333333357 0.6666666666666643 0.6870312235438879
0.6666666666666643 0.3333333333333357 0.5001800687536684
0.3333333333333357 0.6666666666666643 0.3128184006847927
0.0000000000000000 0.0000000000000000 0.7358434371381902
0.0000000000000000 0.0000000000000000 0.6380938495385869
0.3333333333333357 0.6666666666666643 0.5490472923034632
0.3333333333333357 0.6666666666666643 0.4512223851108246
0.6666666666666643 0.3333333333333357 0.3617665706846356
0.6666666666666643 0.3333333333333357 0.2639967722419512

3L: 3R-3R-1

1.00000000000000
3.2538758745571852 0.0000000000000000 0.0000000000000000
-1.6269379372785926 2.8179391681278294 0.0000000000000000
0.0000000000000000 0.0000000000000000 34.0000000000000000
Mo Se
3 6
Direct
0.6666666666666643 0.3333333333333357 0.6869166960348253
0.0000000000000000 0.0000000000000000 0.4999110068979069
0.3333333333333357 0.6666666666666643 0.3131118188156300
0.0000000000000000 0.0000000000000000 0.7357686546318865
0.0000000000000000 0.0000000000000000 0.6380276724950207
0.3333333333333357 0.6666666666666643 0.5488609858990776
0.3333333333333357 0.6666666666666643 0.4510528362167455
0.6666666666666643 0.3333333333333357 0.3620494589005518
0.6666666666666643 0.3333333333333357 0.2643008701083566

3L: 3R-3R-2

1.00000000000000
3.2538758745571852 0.0000000000000000 0.0000000000000000
-1.6269379372785926 2.8179391681278294 0.0000000000000000
0.0000000000000000 0.0000000000000000 34.0000000000000000
Mo Se
3 6
Direct
0.0000000000000000 0.0000000000000000 0.6869268874377781
0.6666666666666643 0.3333333333333357 0.5000243277932034
0.3333333333333357 0.6666666666666643 0.3131098382999878
0.3333333333333357 0.6666666666666643 0.7357375207443512
0.3333333333333357 0.6666666666666643 0.6379868510016720
0.0000000000000000 0.0000000000000000 0.5488823805154048

0.0000000000000000 0.0000000000000000 0.4510746775349331
0.6666666666666643 0.3333333333333357 0.3619977281747658
0.6666666666666643 0.3333333333333357 0.2642597884979041

3L: 3R-3R-3

1.00000000000000
3.2538758745571852 0.0000000000000000 0.0000000000000000
-1.6269379372785926 2.8179391681278294 0.0000000000000000
0.0000000000000000 0.0000000000000000 34.0000000000000000
Mo Se
3 6
Direct
0.3333333333333357 0.6666666666666643 0.6868998615887417
0.6666666666666643 0.3333333333333357 0.5000000000000000
0.3333333333333357 0.6666666666666643 0.3131001384112582
0.6666666666666643 0.3333333333333357 0.7357501433948238
0.6666666666666643 0.3333333333333357 0.6380128419517757
0.0000000000000000 0.0000000000000000 0.5489073783281726
0.0000000000000000 0.0000000000000000 0.4510926216718272
0.6666666666666643 0.3333333333333357 0.3619871580482245
0.6666666666666643 0.3333333333333357 0.2642498566051760

3L: 3R-3R-4

1.00000000000000
3.2538758745571852 0.0000000000000000 0.0000000000000000
-1.6269379372785926 2.8179391681278294 0.0000000000000000
0.0000000000000000 0.0000000000000000 34.0000000000000000
Mo Se
3 6
Direct
0.3333333333333357 0.6666666666666643 0.6868776326313853
0.0000000000000000 0.0000000000000000 0.5000000000000000
0.3333333333333357 0.6666666666666643 0.3131223673686148
0.6666666666666643 0.3333333333333357 0.7356868563508255
0.6666666666666643 0.3333333333333357 0.6379379578296049
0.3333333333333357 0.6666666666666643 0.5488982359431930
0.3333333333333357 0.6666666666666643 0.4511017640568071
0.6666666666666643 0.3333333333333357 0.3620620421703949
0.6666666666666643 0.3333333333333357 0.2643131436491744

REFERENCES

1. Zhao, Y. Y.; Luo, X.; Li, H.; Zhang, J.; Araujo, P. T.; Gan, C. K.; Wu, J.; Zhang, H.; Quek, S. Y.; Dresselhaus, M. S.; et al. Inter Layer Breathing and Shear Modes in Few-Trilayer MoS_2 and WSe_2. *Nano Lett.* **2013**, *13*, 1007-1015.
2. Umari, P.; Pasquarello, A.; Dal Corso, A. Raman Scattering Intensities in Alpha-Quartz: A First-Principles Investigation. *Phys. Rev. B* **2001**, *63*, 094305.
3. Liang, L. B.; Meunier, V. First-Principles Raman Spectra of MoS_2, WS_2 and Their Heterostructures. *Nanoscale* **2014**, *6*, 5394-5401.
4. Aroyo, M. I.; Perez-Mato, J. M.; Orobengoa, D.; Tasci, E.; de la Flor, G.; Kirov, A. Crystallography Online: Bilbao Crystallographic Server. *Bulg. Chem. Commun.* **2011**, *43*, 183-197.
5. Ribeiro-Soares, J.; Almeida, R. M.; Barros, E. B.; Araujo, P. T.; Dresselhaus, M. S.; Cançado, L. G.; Jorio, A. Group Theory Analysis of Phonons in Two-Dimensional Transition Metal Dichalcogenides. *Phys. Rev. B* **2014**, *90*, 115438.
6. Zhao, W. J.; Ghorannevis, Z.; Amara, K. K.; Pang, J. R.; Toh, M.; Zhang, X.; Kloc, C.; Tan, P. H.; Eda, G. Lattice Dynamics in Mono- and Few-Layer Sheets of WS_2 and WSe_2. *Nanoscale* **5**, 9677-9683 (2013).